Earth and Planetary Science Letters 454 (2016) 213–224

Contents lists available at ScienceDirect

Earth and Planetary Science Letters

www.elsevier.com/locate/epsl

Evidence for impact induced pressure gradients on the Allende CV3 parent body: Consequences for fluid and volatile transport

Alastair W. Tait [a,*], Kent R. Fisher [b], Poorna Srinivasan [c], Justin I. Simon [d]

[a] School of Geosciences, Monash University, Melbourne, Vic., 3800, Australia
[b] University of Cincinnati, Cincinnati, OH, 45219, United States
[c] University of New Mexico, Department of Earth and Planetary Sciences, Albuquerque, NM, 87131, United States
[d] Center for Isotope Cosmochemistry and Geochronology, ARES, NASA Johnson Space Center, Houston, TX, 77058, United States

ARTICLE INFO

Article history:
Received 20 April 2016
Received in revised form 7 September 2016
Accepted 8 September 2016
Available online 30 September 2016
Editor: A. Yin

Keywords:
meteorite
petrofabric
lineation
foliation
deformation
fluid

ABSTRACT

Carbonaceous chondrites, such as those associated with the Vigarano (CV) parent body, exhibit a diverse range of oxidative/reduced alteration mineralogy (McSween, 1977). Although fluids are often cited as the medium by which this occurs (Rubin, 2012), a mechanism to explain how this fluid migrates, and why some meteorite subtypes from the same planetary body are more oxidized than others remains elusive. In our study we examined a slab of the well-known Allende ($CV3_{OxA}$) meteorite. Using several petrological techniques (e.g., Fry's and Flinn) and Computerized Tomography (CT) we discover it exhibits a strong penetrative planar fabric, resulting from strain partitioning among its major components: Calcium–Aluminum-rich Inclusions (CAIs) ($64.5\%_{CT}$) > matrix ($21.5\%_{Fry}$) > chondrules ($17.6\%_{CT}$). In addition to the planar fabric, we found a strong lineation defined by the alignment of the maximum elongation of flattened particles interpreted to have developed by an impact event. The existence of a lineation could either be non-coaxial deformation, or the result of a mechanically heterogeneous target material. In the later case it could have formed due to discontinuous patches of sub-surface ice and/or fabrics developed through prior impact compaction (MacPherson and Krot, 2014), which would have encouraged preferential flow within the target material immediately following the impact, compacting pore spaces. We suggest that structurally controlled movement of alteration fluids in the asteroid parent body along pressure gradients contributed to the formation of secondary minerals, which may have ultimately lead to the different oxidized subtypes.

1. Introduction

On Earth, penetrative planar petrofabrics are commonly found inside metamorphosed rocks that have undergone various degrees of stress. These diagnostic fabrics can be used to interpret the magnitude and origin of the stresses that deformed rocks, such as mylonites. Similar fabrics were first reported in meteorites in the 1960s (Dodd, 1965), but have been limited to a few studies since then (e.g., Cain et al., 1986; Gattacceca et al., 2005; Hanna et al., 2015; Watt et al., 2006).

The petrofabrics are generally found in carbonaceous chondrite types CM (Mighei-like) (Hanna et al., 2015; Rubin, 2012), CV (Vigarano-like) (Cain et al., 1986; Rubin, 2012) and some OC (Ordinary Chondrites) (Dodd, 1965; Krzesińska et al., 2015; Sneyd et al., 1988). The fabrics are defined by the alignment of oblate particles (e.g., chondrules and CAIs) implying pure shear (Cain et al., 1986; Sneyd et al., 1985, 1988). Pure shear requires differential stress, the difference between the maximum and minimum stress tensors, and results in coaxial deformation. Geological processes that create pure shear with an even confining pressure have been used to explain the origin of these petrofabrics (Passchier and Trouw, 2005). Early studies favor gravitational overburden to describe the uniaxial shortening, which is due to the apparent unrecoverable viscous textures (Cain et al., 1986; Dodd, 1965). However more recent studies cite evidence for an impact driven mechanism (Bland et al., 2014; Gattacceca et al., 2005; Rubin, 2012; Sneyd et al., 1988).

In addition to planar fabrics, penetrative lineations have also been reported in meteorites (Dodd, 1965; Hanna et al., 2015). However, these lineations have received even less attention by the planetary community than their planar counterparts; they have either been measured but not reconciled (Dodd, 1965), dismissed as being too weak as to affect the interpretation of the petrofabric forming mechanism (Sneyd et al., 1988), or not observed.

* Corresponding author.
E-mail address: alastair.tait@monash.edu (A.W. Tait).

http://dx.doi.org/10.1016/j.epsl.2016.09.015

Table 1
CV Subtype characteristics related to shock.

Name	Subtype	Shock stage[a]	Permeability[b] (m^2)	Matrix porosity[b] (%)	Bulk porosity[b] (%)	Bulk porosity[c] (%)	Planar fabric bulk (R_f)	Lineation
Allende	OxA	S1	$(2.2–52.) \times 10^{-16}$	25	20	21.9	1.45	Yes
Axtell	OxA	S1	–	–	–	23.4	None[g]	?
Mokoia	OxA + Ox B	S1	–	30	24	27.7	–	?
Grosnaja	OxB	S3	–	–	–	–	Strong[e]	?
Bali	OxB	S3	$(2.8–16) \times 10^{-17}$	2	10	–	Well-defined[f]	?
Vigarano	Red + Ox	S1–S2	$\leq 9.4 \times 10^{-17}$	6	2–7	8.3	Moderate[e]	?
Leoville	Red	S3	$\leq 4 \times 10^{-18}$	–	2	2.1	1.82[h], 2.0[d] Strong[e]	?
Efremovka	Red	S4	$(2–3) \times 10^{-18}$	1	7	0.5	Strong[b]	?

Modified table from MacPherson and Krot (2014).
[a] Scott et al. (1992).
[b] Corrigan et al. (1997); relative errors for permeability not given; relative errors for porosity estimated to be ±15% of value shown.
[c] Macke et al. (2011a, 2011b); Errors on individual porosity measurements 1–4% for small samples (mass <90 g) and approximately 1–2% for mass >90 g.
[d] Cain et al. (1986).
[e] Martin et al. (1975).
[f] Keller et al. (1994).
[g] Simon et al. (1995).
[h] Almeida et al. (2015).

Piazolo and Passchier (2002) define lineations into two board categories: 1) "Object Lineations", which are distinct elongate parts of the rock with a measurable volume (e.g., grain lineation, aggregate lineations). 2) "Trace Lineations", which are material lines of zero volume (e.g., intersection lineations, crenulation lineations, shatter cone orientations). Lineations produced by deformation on Earth are of the utmost importance to structural geologists as they are used to show a heterogeneity in all three stress fields, which results in preferred shape orientation along one axis (e.g., Passchier and Trouw, 2005).

An important consequence of lineations on Earth is their control on fluid transport within rocks (Carter et al., 1990; Weinberg et al., 2013). Potential consequences of lineations for chondrite parent bodies include both implied pressure gradients due to compaction, as well as, preferential pathways for fluid transport. In other words, a bolide impact would create a seismic event increasing stress in the rock that exceeds the strength of the rock. Dilation due to rock failure would draw in fluids providing a mechanism for fluid transport (Carter et al., 1990). This could control the transport of magmatic and volatile fluids and/or ductal migration of metal phases. Recently, evidence for such a mechanism was found in the CM2 Murchison chondrite, with cross cutting alteration veins found to be parallel to the foliation (Hanna et al., 2015). In addition, the same study found micrometer scale evidence of volatile transport and alteration in chondrules. The study revealed that the chondrules were deformed internally from an impact, allowing for fluids to infiltrate micrometer scale "pull apart" structures and form serpentines, resulting in an overall flattened appearance of the chondrules. Understanding fluid transport is more difficult in the absence of preserved microstructures. Such observations may be hard to find in higher petrological type specimens. For instance, alteration textures from the CV's or OC's may have been destroyed by high degrees of thermal processing.

In an effort to more universally understand fluid transport on such bodies, our study compared petrofabrics we observed in the CV3 Allende meteorite to microstructures seen in Murchison (Hanna et al., 2015). One consistent observation in CV subtypes is that reduced subtypes have increased shock (S3–S4), $CV3_{OxB}$ types have light to moderate shock S1–S3, and $CV3_{OxA}$ types have low shock (S1) (Scott et al., 1992). Interestingly, there is also a decrease in permeability and porosity with increased shock grade in the reduced subtype (Corrigan et al., 1997; Macke et al., 2011a, 2011b; MacPherson and Krot, 2014; Rubin, 2012) (see Table 1). Some debate exists as to whether the compaction and reduced porosity in $CV3_{red}$ subtypes restricted later alteration (Rubin, 2012), or if the compaction from the impact expelled the fluids out of the pore spaces (MacPherson and Krot, 2014). Evidence for the latter are "dish structures", which indicates that fluid moved through dark inclusions (Tomeoka and Kojima, 1998), but the timing of this fluid migration is still an ongoing debate. One final observation is that the porosity in $CV3_{OxB}$ is lower than $CV3_{OxA}$ despite their higher shock and increased chemical alteration (Rubin, 2012). It should be noted that the vast majority of these observations are qualitative (Keller et al., 1994; Martin et al., 1975; Scott et al., 1992; Simon et al., 1995), using colloquial terms (see Table 1). Among the CV3 meteorites only Leoville and Allende (Almeida et al., 2015; Cain et al., 1986) have had their strain quantitatively measured. Our study aims to add to the quantitative data in the literature.

In this study, we will show that Allende, the archetypical $CV3_{OxA}$ meteorite, does contain a planar, as well as a linear petrofabric. We interpret this to be evidence of mechanical heterogeneity surrounding the point of impact on the parent body, resulting in preferred deformation and a stress field gradient by which fluids could be preferentially mobilized. Additionally, we discuss recently proposed non-coaxial deformational models (Krzesińska et al., 2015). Such a formation history might help explain the distinct alteration histories among the CV3 subtypes, although it is complicated by radiogenic heating (Doyle et al., 2015; Wasson et al., 2013). This conclusion is reached through detailed study of a slab of Allende (~27 cm × ~20 cm × 5 mm), using conventional 2D strain analysis techniques, in conjunction with X-ray Computerized Tomography (CT). These novel observations are discussed in terms of how the lineation fits into current petrofabric formation ideas and ultimately what these observations may mean for fluid and volatile transport on chondrite parent bodies.

2. Methods

For this study a ~25 cm^2 slab of the Allende CV3 meteorite was chosen due to its uniquely large size (Fig. 1). Most geological discrimination of textures and mineralogy is done using thin sections. If not carefully integrated with outcrop scale observations, such studies can introduce a sizing bias by emphasizing local thin section scale mineralogical/textural heterogeneities to the overall system (Palin et al., 2015). Meteorite analysis is no different, and observation on thin sections could make observers miss larger trends and extrapolate smaller heterogeneities to the whole parent body. This slab provides a unique opportunity in meteoritics to minimize this bias by allowing for an order of magnitude larger petrographic discrimination. It is worth noting that the parent mass of the sample used was cut into slabs for meteorite collectors long before this study. As such we had no control of where the

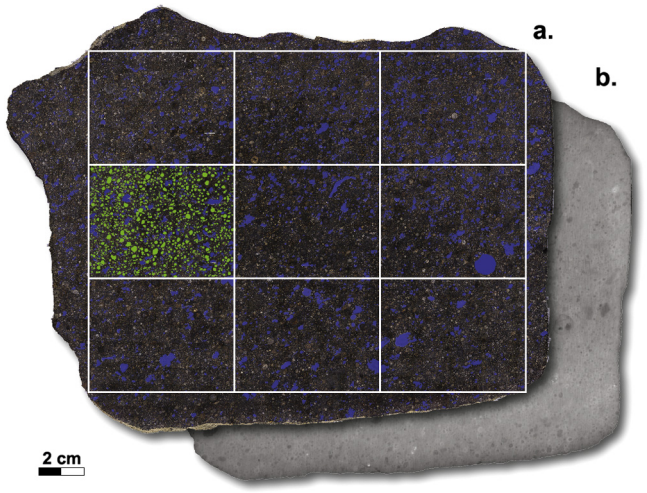

Fig. 1. Sample overview: (a) Image shows the photomosaic slab of Allende CV3 at a resolution much lower than then the 13.88 μm/px used for analysis. The largest rectangle containing the 9 smaller cells is the *Large* dataset. The smaller cells were tested for overall similarity to the *Large* dataset using the CAIs (digitized in blue). The Cell that also includes green digitized chondrules and their rims is Cell 4, the *Medium* dataset (see text). (b) A representative image of the computed tomographic (*CT*) dataset for comparison. The stacked dataset has a 1:1:1 voxel resolution of 173.91 μm/voxel. Both the *CT* data and the photomosaic slab of Allende were aligned with the top of the image being north (0°). (For interpretation of the references to color in this figure legend, the reader is referred to the web version of this article.)

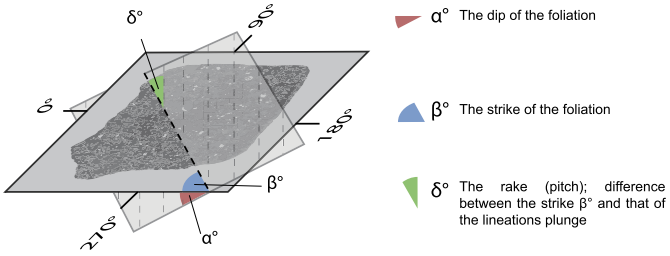

Fig. 2. Foliation and lineation orientation: (a) This image shows the slab of Allende worked on in this study. Projected into this slab is the orientation of the petrofabric revealed by our analysis. The semi-transparent plane represents two fabrics; the foliation (intersecting plane) and the lineation (dashed lined) in the slab, with respect to an arbitrary orientation (reference frame), the top of the slab being angle 0°. Angle ($\alpha°$) is the dip of the foliation, angle ($\beta°$) is the orientation of the strike, and angle ($\delta°$) is the rake; difference between the angle $\beta°$ and that of the lineation's plunge. For point of reference frame with the *CT* data set, both it and the photomosaic slab of Allende were aligned with the top of the image being north (0°).

cuts were made with respect to the observed foliation/lineation, and as such, any strain analysis from the 2D photomosaic data set should be considered to represent the minimum amount of strain, and not absolute, with the exception of the *CT* dataset. For clarity, we discuss the sample in one orientation throughout and report all measurements with respect to this orientation. This is shown in Fig. 2 where the main face of the cut sample is flat. We defined three angles in order to describe a pervasive foliation plane in the meteorite and a lineation defined by the deformed particles. Angle ($\alpha°$) is the dip of the foliation, angle ($\beta°$) is the strike of the foliation, and angle ($\delta°$) is the rake (pitch); difference between the angle $\beta°$ and that of the lineation's plunge.

2.1. Photographic data set preparation

To evaluate the petrofabric of the Allende slab, we photographed both sides of the slab using a camera attached to an optical microscope. Images were acquired in a grid pattern with a mechanical stage at a resolution of 13.88 μm/pixel (Fig. 1). Approximately 10% overlap was used when obtaining images, which provided accurate stitching in Adobe Photoshop to create the two mosaics of the slab; both the top and bottom were stitched and comprised of ∼400 images each. In order to analyze the fabric in Allende, we were faced with the prospect of manually digitizing thousands of particles. To save time CAIs were digitized first due to their smaller modal abundance compared to chondrules. Constituent CAIs within the mosaics were outlined on both sides using a large digitizing art board. To cut down on the amount of digitization necessary, we divided the previous slab into 9 equal area rectangles called "cells", both on the front and the back Fig. 1. The long axis length of CAIs was taken as a measure of similarity. This shape descriptor is easily calculated in ImageJ, and is a good measure for the size distribution of particles (Simon et al., in preparation). CAI lengths within the cells were measured based on their arithmetic-mean, median, standard-deviation and sample variance, and this was calculated for both sides of the slab. Each cell also had the same statistical measures recorded. These were expressed as a percentage difference from the overall statistical measures, which were finally averaged between the values from the top and bottom (Supplementary Table 2). Despite all cells recording little variation, cell 4 was chosen as representative of the whole slab, as it recorded the lowest difference from the overall dataset in three out of the four statistical measures we used.

For simplicity, all sub-groups of particle types were consolidated into larger groupings. All chondrule types (e.g. Porphyritic Olivine-Pyroxene, Radial Pyroxene, etc.) were grouped as "chondrules". All types of refractory inclusions (including Amoeboid Olivine Aggregates (AOAs)) were designated as "CAIs". The representative rectangular Cell 4 sub-section of the slab was rotated clockwise 0°, 90°, 180°, then characterized independently by authors A.T., K.F., J.I.S. to quantify the distribution, shape, size, and orientation of all particles that make each of these two component populations. The purpose of this was to evaluate potential bias and variation that may occur from drawing styles and different levels of petrographic experience among workers. This Cell 4 sub-section containing digitized chondrules and CAIs will be referred to as the *Medium* dataset, whereas the CAI data from the overall slab, which Cell 4 was found statistical similar will be referred to as the *Large* dataset. This study will focus on the *Medium* and the *CT* datasets.

2.2. Computerized Tomography (CT) data set preparation

The slab underwent computerized tomography at NASA Johnson Space Center (JSC), using a Comet 450 source with a Perkin Elmer 1621 detector (200 μm pixel size), running at 450 kV and 1.55 mA (e.g., McNamara et al., 2010). The focal spot was 400 μm using a 0.1" Cu filter. The achieved voxel resolution for the experiment was 173.91 μm/pixel. The acquisition was done at a magnification of ×1.15 with 1440 projections over a 360° range, and an angle step of 0.25°. Frame rate was 2 fps, with a frame average of 4 frames. The duration of the experiment was 2 h, 3 min and 25 s, after which the data was sharpened. After acquisition, the images slices were smoothed by Non-Local Means (NLM), using the Adobe Photoshop® plugin Ximagic v4.8. This smoothing technique accentuates the edges, while smoothing out the intervening information. This makes analysis of shape descriptors clearer. Due to the similarity in density of chondrules and the matrix, the Look Up Table (LUT) had to be scaled to resolve the two components before analysis. Their distinction was confirmed by comparison to the 2D *Large* data set where the CAIs and chondrules exposed at the surface are clearly distinct. The computerized tomography (*CT*) dataset was aligned with the photomosaic datasets to make sure all values being discussed are in the same reference frame.

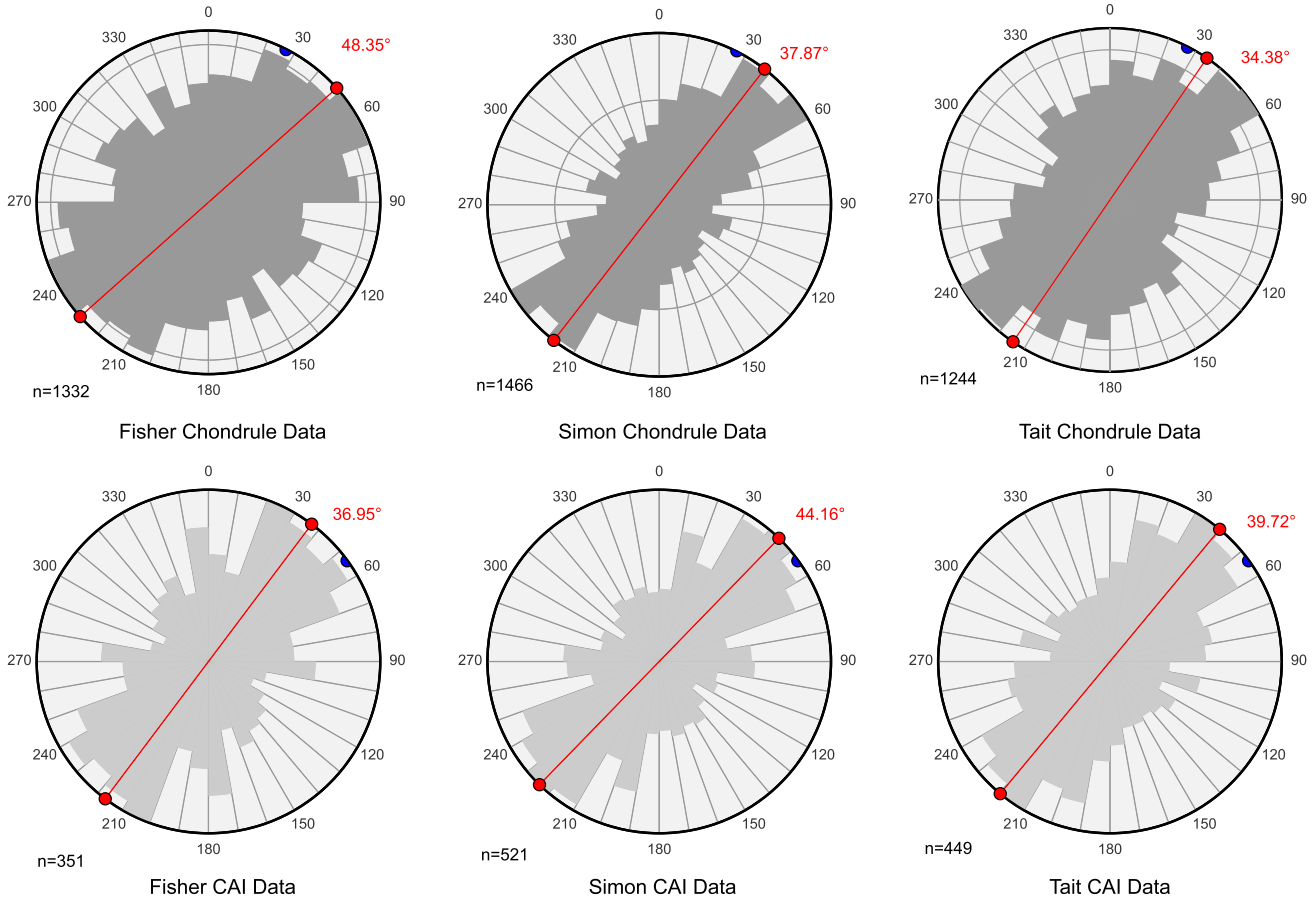

Fig. 3. Rose diagrams displaying particle orientation measured by multiple observers. Each plot shows the dominant angles of the long axis of chondrule and CAI particles in the *Medium* data set, binned at 10°. To account for human bias when digitizing, the particles were digitized three times by three of the authors (Tait, Simon, Fisher) and at different sample orientations. The red dot on each rose diagram is the mean apparent-strike for the particles, and is calculated from the maximum eigenvalue. The blue dot is the lineation trend of the particle phase as determined from stereonet and *CT* data (see text). The agreement shows that integration of data collected by multiple observers and 2D analysis and 3D analysis lead to minimal systematic uncertainties in the *Medium* data set. (For interpretation of the references to color in this figure legend, the reader is referred to the web version of this article.)

2.3. Finite strain analysis

This study uses methods carried out in previous meteorite petrofabric papers (Cain et al., 1986; Sneyd et al., 1988). The strain ellipsoid is a common technique in structural geology used to evaluate the kinematics related to deformation in a rock. Particles in the sample show an apparent shortening along one axis, consistent with what is seen in the previous papers using this method (Cain et al., 1986; Sneyd et al., 1985). We used the digitized chondrules and CAIs of each author's sub-section and compared them using the particle function of the ImageJ software, which fits an ellipse to each particle (Schneider et al., 2012). Important shape descriptors recorded from these fitted ellipses were 1) major/minor axis and, 2) the angle of the major axis in a reference frame where the top of the image is defined as 0° (see angle β° in Fig. 2). Harmonic means were used to reduce the influence of outliers on the gathered datasets. The axial-ratio (R_f), which is the ratio of the major and minor axis lengths, was converted to a Uniaxial Shortening (U_s) ratio using the following equation (1) (Hanna et al., 2015):

$$U_s = 1 - R_f^{\left(-\frac{2}{3}\right)} \tag{1}$$

However, this equation comes with some caveats (Hanna et al., 2015): the strain is 1) entirely uniaxial (coaxial, non-rotational), 2) only describes particles that maintain their volume and are not compressible, 3) only describes the deformation of particles that were initially spherical. Particles that are brecciated or irregular CAIs will result in significant scatter about a linear regression. Chondrites are not perfect systems, as they contain a heterogeneous mix of distinct materials. Values derived from equation (1) should only be considered as semi-quantitative. The orientations of the particles were plotted using rose diagrams (Fig. 3). This was done in order to determine if there was a preferential orientation of the particle's long axis.

2.4. Fry's method

We used Fry's Method to quantify the amount of strain in the matrix. This is a center-to-center technique for establishing the amount of whole rock finite strain (Fry, 1979). For optimal results, anti-clustered samples such as sandstones and conglomerates are usually chosen, however, chondrites also fit this requirement due to their aggregate nature. To reduce ambiguity, we used an objective fitting algorithm for Fry's method (Waldron and Wallace, 2007). This was run through ImageJ on each of the *Medium* chondrule datasets after the data was returned to a common orientation. Chondrules were used for this technique due to their higher resistance to deformation in a porous matrix. They also have a more coherent crystalline nature, and therefore should be more representative of whole rock deformation.

2.5. Flinn's method

Flinn's method records the change in length of the major axis of a 3D particle by graphing the axis as a ratio $a = Z/Y$ and

$b = Y/X$, where the length of axis is $Z > Y > X$ (Flinn, 1962). Under ideal conditions when a sphere is deformed into an ellipsoid, the maximum and minimum axial shortening directly correlates to the volume conserved. It is possible with Flinn's method to plot a straight deformation path with the shape descriptor 'k', defined as:

$$k = \frac{a-1}{b-1} = \frac{X(Z-Y)}{Y(Y-X)} \quad (2)$$

where $k < 1$ connects the fields of all oblate uniaxial ellipsoids, and $k > 1$ connects the fields of all prolate uniaxial ellipsoids. Relative to most computerized tomography scanning investigations the sample slab is very thin (~5 mm). The thickness represents one chosen by the meteorite dealers who cut it. For the purpose of this study, great care was taken to ensure that all CAIs ($n = 19$) and chondrules ($n = 10$) evaluated were fully encapsulated by the slab, as particles that are at the surface are truncated and would lead to bias. As such, encapsulated particles are smaller than 5 mm in diameter. Because density contrasts between chondrules and CAIs were similar, LUT (look up table) discrimination required manual input. Shape and textual properties were employed to determine the difference between chondrules and CAIs (Supplementary Figure 3) and were tested by comparisons to the *Large* data set. Target particles were then cropped in place to preserve orientation and stacked in ImageJ and exported to Adobe Illustrator for digitizing. Once this was completed, an 8-bit image for each CT particle scan slice was exported at the same resolution to conserve scale and orientation. The ImageJ plugin BoneJ was then used to turn the image stack into a 3D model (Doube et al., 2010) (Supplementary Figure 1). Although this is primarily used for medical research, the ellipsoid fitting of simple particles is useful for this study. The program BoneJ fitted an ellipsoid to each particle in the stack and shape descriptors were recorded: 1) axial-lengths and 2) component vectors of the primary axis. The axial lengths were used for Flinn's method to establish the deformational regime, and the axial orientation of the primary axis was used to evaluate the existence of a lineation. The component vectors of the primary axis were converted to trend/plunge format and plotted on a stereonet. For more information on this method see Supplementary information 1.1.

3. Results

3.1. 2D strain analysis: rose diagrams

Using the particle analysis tool in ImageJ, we measured the orientations from the long axis of the *Medium* dataset (with the top of the slab at 0°), making sure not to include any particles that intersected with any of the slab edges. This process was repeated three times by different authors at 000°, 090° and 180° rotations. The results are shown using rose diagrams, and were subdivided into 10° bins (Fig. 3). We obtained similar mean vectors (red line in Fig. 3) for each dataset, reflecting the uniform strike of the long axis between particle types. The arithmetic mean calculated from the three datasets is: Chondrule(ϕ) = 040.02° ± 7.27° SD, and CAI(ϕ) = 040.28° ± 3.64° SD. The number of particles digitized by the authors are: Chondrules(n) = 1347.33 ± 111.79, and CAI(n) = 437.33 ± 81.13.

By using different observers to digitize the sample we were able to evaluate the effect of human biasing on the results. When determining the angle of the particles, the standard deviation for the chondrules was 7.27°, which translates to a spread of 18.1% of the mean. This compares to a spread of 9.0% for the CAIs. This is likely because CAIs record higher deformation than the somewhat circular areas of chondrules (see below), resulting in sharper and clearer orientations. Also, the number of chondrules and CAI particles that were digitized differed from worker to worker; this resulted in a total difference from the mean of 8.3% and 18.6% for chondrules and CAIs, respectively, between observers. This is probably due to human factors resulting in difficulty determining the difference between a chondrule/CAI/AOA from a static color photo at the smallest sizes, and thus mainly due to the willingness of the observer to digitize at the smaller sizes (i.e., experience and diligence led to measurement of more of the smallest particles). Nevertheless, there is a clear strike towards ~040° in both particle datasets relative to the north-oriented (to 000°), crudely rectangular slab (Figs. 1, 2).

3.2. 2D strain analysis: particle deformation

Using the same data sets from each of the observers, an ellipse was fitted to the particles using ImageJ. This defined the length of the major (X) and minor (Z) axes of the particles. The lengths of these two axes were plotted and fit by a linear regression. The results from the 2D strain analysis are presented in Supplementary Figure 2, which also includes the axial deformation (R_f; the gradient from the line of best fit). In regards to the ratio of axial deformation, the arithmetic mean calculated from the datasets of the three observers is less than before: Chondrule (R_f) = 1.33 ± 0.03 SD, CAI (R_f) = 1.67 ± 0.05 SD. The standard deviation for the means expressed as a percentage for the chondrule (~2.3%) and the CAI (~3.1%) datasets is minimal. The R^2 values from each worker were calculated and averaged together. Both the chondrules and CAIs have relatively high R^2 values: (R^2) = 0.82 ± 0.01 SD and (R^2) = 0.80 ± 0.01 SD, respectively. Chondrules were likely initially spherical as compared to the unknown starting eccentricity of the CAIs (Martin and Mills, 1976; Sneyd et al., 1988). Regardless, such a high R^2 value indicates a very uniform level of strain across the slab, as a consequence of uniform stress. Assuming that all particles were initially spherical (which may not be the case for CAIs), extrapolating the ratio of axial deformation to percentage of uniaxial shortening (U_s) show that the chondrules have undergone 17.45% ± 7.09% of shortening, compared to the CAIs which have undergone 28.91% ± 5.12% of shortening.

3.3. 2D strain analysis: Fry diagram

To understand the amount of stress taken up by the matrix a center-to-center deformation method was used. This is employed because chondrules are crystalline and less likely to deform than "fluffy" type CAIs or fine-grained matrix. This approach may give a better overall account of whole rock deformation. Chondrules were digitized with their rims and measured using Fry's method (Fig. 4). The average axial ratio (R_f) was 1.45 ± 0.16, which translated to a uniaxial shortening (U_s) for the matrix of 21.50% ± 5.44%. Compared to the other 2D strain analysis, this is more than the chondrules and less than the CAIs. However, it should be mentioned that this data has the largest worker induced standard deviation of 25.31%. Nevertheless, the strike of the fitted ellipse results in the matrix(ϕ) = 037.07° ± 4.74°, which overlaps the strikes of the chondrules and CAIs (Fig. 3).

3.4. CT strain analysis: particle deformation

The ellipsoid shape descriptors from the *CT* analysis can be seen in Supplementary Table 1. These show that the chondrules underwent 17.56% ± 3.27% uniaxial shortening, which is in excellent agreement with the 2D strain result of 17.45% ± 7.09%. Contrastingly, the *CT* analysis showed the CAIs underwent 64.56% ± 7.52% deformation, but the 2D strain analysis result was 28.80% ± 1.47%. This is quite a large difference between the 2D and *CT* datasets for the CAIs. Several factors in combination likely explain the disparity between the 2D and the *CT* datasets for CAIs. These include: 1) The *CT* data set represents a smaller sample size; this may have lead to

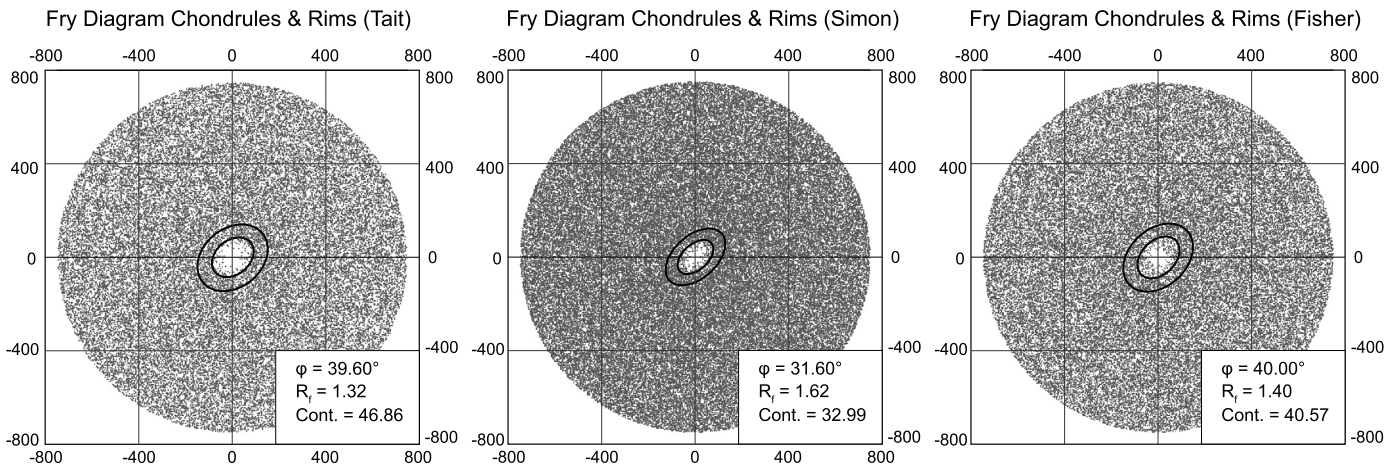

Fig. 4. Fry diagrams of chondrules with their rims measured by three people. These images show the inter-particle spacing relationships. Chondrule and their rims were chosen due to their crystalline structure and thus more likely to act as porphyroblasts that resist deformation assuming that they were initially equal or randomly distributed. This approach provides a useful indication of whole rock (i.e., matrix) deformation. Phi (symbol) is the strike of the strain ellipse, R_f is the axial ratio (values above 1 indicate elongation), and contrast (Cont.) is a measure of fit of the annulus, larger values are better (Waldron and Wallace, 2007).

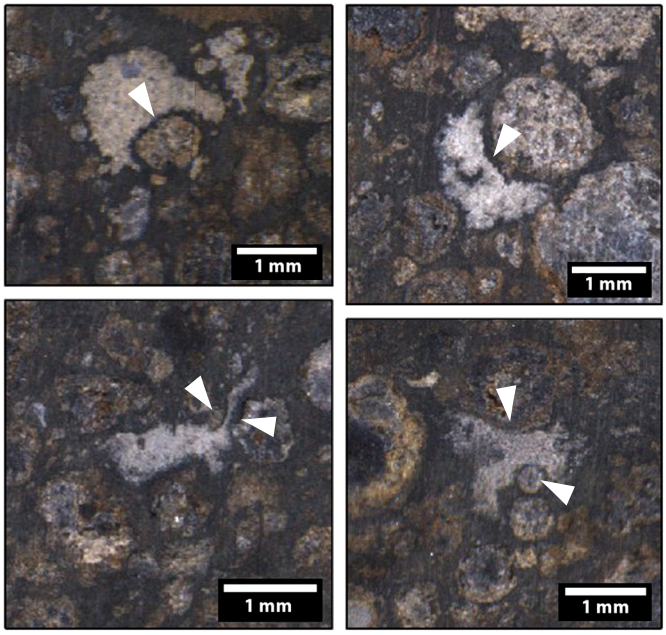

Fig. 5. CAI strain partitioning. This series of images show plastic deformation of fluffy type CAIs around more mechanically competent chondrules and igneous type CAIs. Arrows point towards boundaries that are wrapping around more competent grains.

an amplification of outliers. 2) On average, the particle sizes of the CAIs measured by *CT* are smaller than those measured in the 2D dataset. These smaller CAIs may show more increased deformation or irregularity than larger ones. This could be because the smaller CAIs can be "engulfed" within the porosity of the pre-impact matrix and more readily deformed (see below). 3) The 2D CAI dataset defines a minimum degree of deformation due to the cut of the sample that is accentuated by the more elongated shape typical of CAIs. Nevertheless, it is notable that the disparity between the amounts of chondrule and CAIs deformation can be seen in the slab, whereby CAIs are found wrapping around more competent chondrules (Fig. 5).

3.5. CT strain analysis: particle axial length

The maximum axial length (X) was plotted against the minimum axial length (Z) for both the chondrules and CAIs (Fig. 6). The chondrules show near uniform deformation with an $R^2 = 0.96$. This is a remarkably good fit, much better than the 2D strain analysis. This result is similar to other work that shows that chondrules share a similar starting ellipticity (Hanna et al., 2015; Sneyd et al., 1988). Also, due to the low fluctuation around the linear trend, we can infer that they underwent near uniform deformation across the ~25 cm^2 slab. The CAIs however yield an $R^2 = 0.23$, which is probably due to the fact that the shape of CAIs prior to their parent body accretion were already irregular in shape, or at least some were, and also likely due in part to their granular rheology, possibly squeezing into empty pore spaces and wrapping around more competent chondrules (e.g. Fig. 5).

3.6. CT strain analysis: Flinn diagram

To characterize the shape of the strain ellipsoid we plotted the major (X), intermediate (Y), and minor (Z) axis of both the chondrules and the CAIs on a logarithmic Flinn graph (Fig. 7). The graph shows that the majority of the CAIs plot in the oblate field. This is the field whereby particles form "pancake" shapes. The graph reveals a shape descriptor $k = 0.45$ for CAIs and $k = 0.91$ for chondrules. The formation of the two particle populations likely depends in large part on the rheology of the particles; CAIs are more granular, whereas chondrules are more crystalline, leading to different deformation regimes and resistances. Some of the chondrules plot in both the oblate and the prolate field; the prolate field is where particles form "cigar" shapes. There is an outlier from the CAIs in the prolate field. Nevertheless, most particles plot in the oblate field with axis $X \neq Y$ in length, indicating the possibility of preferred orientation (see below).

3.7. CT strain analysis: Stereonet

To further evaluate the possibility of a preferred orientation, the particles used in the previous section had the directional cosines of their primary axis converted to trend and plunge, which was then plotted onto an equal area spherical projection map (Fig. 8a). We observed that the long axis of both the chondrules and CAIs plunged towards a common point, which we interpret to be a lineation. We used the program Stereonet v9.3.2 (Allmendinger et al., 2012; Cardozo and Allmendinger, 2013) to quantify the tightness of the data for the lineation and calculate a Fisher Mean distribution (Fisher, 1953). The Stereonet program produces a mean trend/plunge and the Fisher precision parameter *k*. This *k* value can

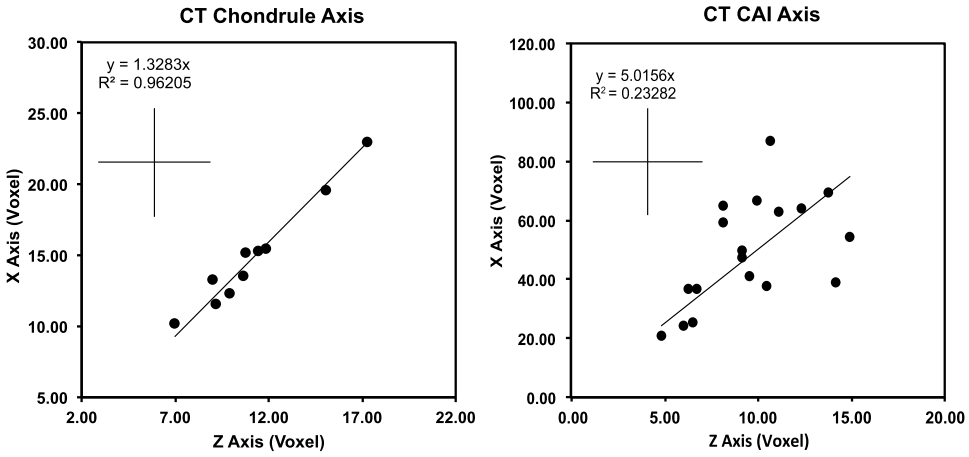

Fig. 6. CT particle axis length comparison. These graphs show the long (X) and the short (Z) axis derived from ellipsoid fitting of particles from the *CT* dataset. The chondrules show an elliptical shape consistent with near uniform deformation, $R^2 = 0.96$, compared the CAIs that exhibit larger scatter with an $R^2 = 0.23$. The discrepancy between the two data is most likely due to the different starting elliptical shape of the CAIs compared to the more uniform chondrules. The cross represents 1σ errors.

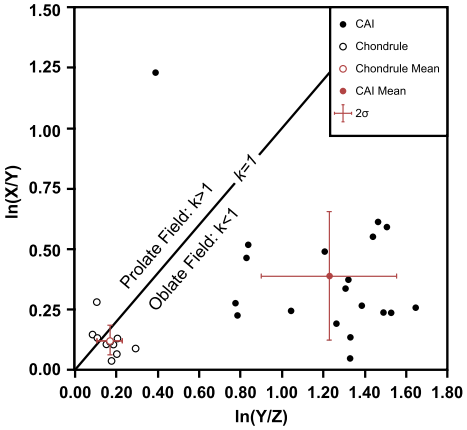

Fig. 7. Flinn diagram. This diagram shows that the CAIs (solid circles) plot strongly in the oblate field. The spread is most likely an artifact of their irregular starting shapes. The arithmetic mean has the shape descriptor value of $k = 0.45$, with error bars at 2σ. One outlier plots in the prolate field. The chondrules (open circles) are much more tightly distributed with an arithmetic means shape descriptor value of $k = 0.91$, with error bars at 2σ.

be used to estimate the angular standard deviation (also known as the angular dispersion "s"), as well as be used to calculate varying cones of confidence. The angular dispersion can be calculated using the following equation (Butler, 1992):

$$s \approx \frac{81^\circ}{\sqrt{k}} \tag{3}$$

where "s" is the angular standard deviation and k is the Fisher precision parameter. The chondrules had a mean trend and plunge of 027.1°/−21.6°, a Fisher precision parameter k value of 2.3, and an angular standard deviation of 53.4°. The CAIs had a Fisher Distribution trend and plunge of 054.3°/01.1°, a k value of 3.8, and an angular standard deviation of 41.6°. The range of plunges for the chondrules and CAIs overlap with each other, indicating a linear feature. These values are shown as blue dots with the 2D data in Fig. 3 revealing excellent agreement between the 2D data and the 3D dataset. The shallow plunges of the CAIs indicate that the meteorite slab was cut very close along the trend, seen in Fig. 8b. In addition to the lineation, the CAIs form a line of values along a plane (Fig. 8b), with a strike and dip of 056°/17°N. This is evidence of a foliation with lineations fanning around their mean plunge orientation.

4. Discussion

4.1. The existence of a fabric in Allende

This study combined several 2D and 3D techniques to quantify the petrofabric in the Allende CV3 meteorite. The cut slab and the *Medium* sample area generated three data sets: 1) Chondrule and CAI strain analysis (Supplementary Figure 2), 2) Rose diagrams (Fig. 3), and 3) Whole rock strain using Fry's method (Fig. 4). From the data, we infer that the chondrules and CAIs both have a strike defined by the orientation of particle long axis of ~040° (angle β°, Fig. 2) relative to the top of the slab with a standard deviation less than 8° and 4°, respectively. This apparent preferred orientation is bolstered by the observation that all particles, including the chondrules, have undergone shortening, although the chondrules are less deformed than the CAIs. In addition, the whole rock deformation data inferred from Fry's method shows that the particles have been pushed together along one axis and pushed further apart perpendicular to that shortening axis. The long axis of the annulus generated (Fig. 4) lines up with the ~040° orientation on the slabs reference frame. This demonstrates that the whole rock deformation obtained using Fry's method also has the same orientation as the chondrules and the CAIs strike. This implies that much of the deformation is taken up by particles moving in response to a common stress field.

To determine if the deformation is coaxial or non-coaxial (e.g., Pułtusk ordinary chondrite (Krzesińska et al., 2015)), we need be able to tell the shear-sense (e.g. delta/sigmoid porphyroblasts, rotated particles). This is best achieved if the cut face is *parallel to the lineation and perpendicular to the foliation*. However, as previously mentioned, the collectors cut may not be ideal. To evaluate if the cut face is adequate for shear sense identification we need to establish the orientation of the fabric to the cut face.

To address the question of shear-sense we used the 3D *CT* tomography. From the *CT* data we generated the following results: 1) Rose diagram strike data (Fig. 3), 2) stereonet plotting the trend and plunge of the resultant lineation (Fig. 8). 3) The dip of the foliation inferred from the fan of lineations (Fig. 8). The dip of the foliation associated with the CAIs (angle β° in Fig. 2) is defined by the fan of CAI plunges, that of 17°. Such a shallow dip is not ideal for determining shear sense. Ideally, the dip should be perpendicular to determine shear sense. The trend of the chondrules and CAIs plotted on a stereonet are 027.1° and 054.3°, respectively (Fig. 8), which is different from the strike determined by the stereonets of ~40°. The difference between the plunge of the lineation and the strike of the foliation is the rake (angle δ° in Fig. 2). From

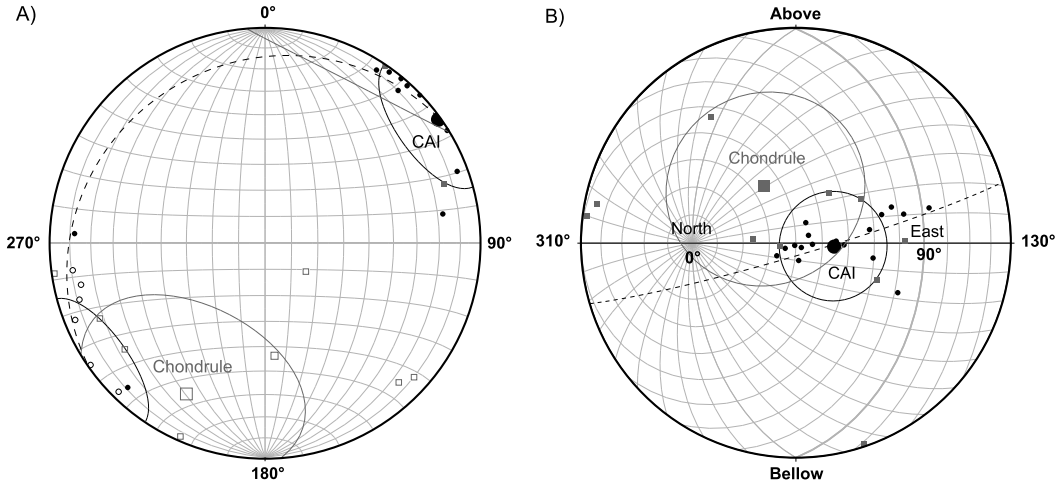

Fig. 8. Stereonet of chondrule and CAI particle orientation. (a) An equal area lower hemisphere stereonet with the trend and plunge of the long axis (relative to the top of the slab). This plot was generated from the ellipsoids fitted to particles in the *CT* dataset. Negative plunges that would plot above the lower hemisphere are converted and plot in open symbols on the lower hemisphere. A Fisher vector distribution was calculated for the CAIs (circles) with a mean trend (larger circle symbol) and plunge of 054.3°/01.1°, with a K value of 3.8, which translates to an angular standard deviation of 41.6°. The circle around the mean is a 95% cone of confidence. The chondrules (squares) define a mean Fisher vector (largest square) trend and plunge of 027.1°/−21.6°, with a K value of 2.3, which translates to an angular standard deviation of 53.4°, the circle around the mean is a 95% cone of confidence. The dotted line is a plane (056°/17°N) defined by the linear arrangement of plunges associated with the CAIs, indicating that the lineation plunges fan out on a plane. The angle 0° is the arbitrarily assigned "North" reference frame, with respect to the aligned *CT* and photomosaic datasets. (b) The same datasets with a reoriented stereonet (040°/00°). The dark solid line represents the surface of the slab. From this point of view, we can see that CAIs mean plots sub-horizontal to the slab, and the chondrules mean plot above the slab, indicating that the overall plunge of the slab is near parallel to the cut face. From this orientation, the linear feature of the CAIs is easier to see and defines the foliation (dotted line).

the rake we can get an idea as to the orientation of the lineation to the cut face. Since the cone of confidence is larger on the chondrules in the stereonet (e.g., due to their round shape) we use the CAIs mean plunge of 1.1°. One can see that it is essentially horizontal to the cut plane, which is essentially zero, thus making the calculation of the rake equal to the angular difference between the trend (as plunge is negligible) and the strike. Therefore, the rake is 14.1° S off the strike (angle δ° in Fig. 2). This means that the cut is, for all intents and purposes, parallel to the trend of the lineation. Although, the lineation is near parallel with the cut face, the foliation is not perfectly perpendicular, but rather sub-parallel (∼17°N), making a determination of shear-sense difficult. No shear sense indicators (e.g. C-S fabric, delta/sigma porphyroblasts) were observed, but the low angle makes their determination difficult and cannot be fully ruled out. Nevertheless, the lack of indicators means that deformation by pure-shear is more likely than simple-shear. This provides additional support that the deformation was coaxial, but does not fully rule out non-coaxial deformation. Perhaps now that such fabrics have been found in Allende, a sample could be more appropriately cut in order to clarify the issue of shear sense.

Although such compelling textural evidence has never before been reported in Allende, we argue that the measured fabric, and thus the implicit meteorite structure, is genuine (i.e., is not an artifact of our imaging techniques) for three reasons: 1) The composite images that generated the 2D photomosaic dataset was collected on a mechanical stage with low magnification to eliminate "fish eye" distortion and had significant overlap. 2) This dataset was overprinted on a CT slice, which was acquired as a single image, to make sure that the stitching was indeed uniform. 3) If the fabric was an artifact, then there should be no reason other than chance that the long-axis of particles from two separate datasets collected by different methods (petrological and *CT*) would yield such good agreement.

From the discussion above we summarize the following structural properties of Allende: 1) There is a foliation. 2) There is a lineation. 3) The lineation is defined by the long axis alignment of oblate grains. 4) There are no visible shear-sense indicators that indicate simple shear, although the cut angle would make them hard to detect. 5) The interparticle distance indicates that particles have been pushed together while being pulled apart perpendicular to that axis. 6) Both the chondrules and the CAIs are deformed. 7) The CAIs are more deformed than the chondrules and matrix.

4.2. Strain localization and deformational regime

Planar fabrics are well known in other CV subtypes (Cain et al., 1986; Martin et al., 1975), some OCs (Sneyd et al., 1988), and CMs (Hanna et al., 2015). Impacts have been used to explain the fabrics (Hanna et al., 2015; Sneyd et al., 1985) due to shear sense indicators and the oblate nature of the particles, but over burden has also been cited (Dodd, 1965). Previous investigations have concluded that the Ox_A subtypes, for which Allende is a member, do not contain a macroscopic planar petrofabric (e.g., Rubin, 2012). It follows that the identification of a planar fabric, and additionally a lineation, in Allende has important consequences for the other CV3 subtypes, many of which have documented, or likely contain undocumented petrofabrics. Despite the lack of documented macroscopic fabrics, microscopic fabrics have been previously observed in the matrix of Allende forming "augens" of secondary pyroxene and olivine around chondrules (Watt et al., 2006). The latter work shows that the amount of strain recorded in the matrix changes based on the distance to more resistant particles, indicating that the amount of strain is not homogeneously expressed in the sample. This is very similar to our results that show that there is an apparent order to the amount of deformation; CAIs ($64.5\%_{CT}$) > matrix ($21.5\%_{Fry}$) > chondrules ($17.6\%_{CT}$), with the CAIs recording the greatest degree of deformation (assuming a spherical starting point). Interestingly, the CAIs also show the greatest degree of deformation in the *Medium* dataset values, $28.91\% \pm 5.12\%$. The discrepancy between the *CT* and *Medium* dataset is fairly large, but it may be due to the sizes of the CAIs documented in the *Medium* dataset vs. those in the *CT* dataset. The CAIs in the *CT* dataset are no more than ∼5 mm in size. As such, there are two issues relating to porosity that could account for this result. Many subtypes of CAIs are aggregates of highly refractory minerals, containing their own porosity (Kornacki and Wood, 1984). Such inter-

nal porosity would make them compressible, as is seen in some chondrules in the Murchison CM2 chondrite (Hanna et al., 2015). This would result in filling their own pore space first, distorting the particle, in response to compression. When these particles are no longer compressible, they would flow into neighboring voids, essentially becoming a pseudomorph of that pore space. It is notable that Allende still has 20% porosity (Corrigan et al., 1997), and likely started with more (Bland et al., 2011). The smallest CAIs ($\ll$5 mm) should therefore flow into pore spaces more readily and deform more easily than more rheological competent chondrules (e.g. Fig. 5). This would create scatter in the dataset and lead to exaggerated deformation in the smaller particles as they fill pore spaces where their entire volume is readily affected by deformation. We interpret that the CAIs are less competent than the surrounding matrix (perhaps due to higher porosity) and much less competent than the surrounding chondrules. This leads to more strain being partitioned into the CAIs, on a whole. This strain partitioning has already been modeled for the CV parent body, but this work focused mainly on chondrules and the matrix (Bland et al., 2014).

Texturally, a CAI could deform more than the chondrules because of their granular composition. Chondrules are mostly crystalline, whereas 'fluffy' type CAIs and AOAs are composed of aggregates of fine- to coarse-grained particles (Kornacki and Wood, 1984; MacPherson and Grossman, 1984). It is much harder to deform a crystal (e.g., Chondrule) through intercrystalline processes with a lattice preferred orientation (LPO) than an aggregate mass of fine-grained material (e.g., Fluffy CAIs & AOA), as a fine-grained mass would deform by extracrystalline processes such as Grain Boundary Sliding (GBS) (Passchier and Trouw, 2005). Such a process would prevent, or even eliminate, the presence of a LPO in the mineral aggregates (Passchier and Trouw, 2005). In addition, the high porosity of this meteorite (>20%) (Corrigan et al., 1997) would indicate the occurrence of a large amount of deformation, as material fills up the empty space in the porosity. Thus it is likely that at least the fine-grain porous CAIs act as "antiporphyroblasts" whereby the CAIs are weaker than the surrounding matrix. This conceptual model is an over simplification of the diversity of chondrule and CAI types and does not take into consideration the possibility of nebular deformation, e.g., the reported effects seen in fine-grained-rims (Bland et al., 2011) or plastically-deformed igneous CAIs (Ivanova et al., 2014). Furthermore, CAIs exhibit different grain sizes and not all chondrules are purely crystalline, some are cryptocrystalline, and many are porphyritic. The latter can lead to internal deformation of the mesostasis (Hanna et al., 2015) resulting in ellipsoid chondrules forming under brittle deformation. Nevertheless, the model can explain the observations for variable strain partitioning in parent bodies, and may also help explain why many CAIs appear to be preferentially deformed (e.g., Fig. 5).

4.3. Impacts on the CV parent body

Ideally, impacts produce uniaxial deformation and purely oblate particles (Cain et al., 1986; Gattacceca et al., 2005; Rubin, 2012). Although this is an over simplification of the high pressure gradients created during the compression stage of an impact it is a useful conceptual model (Melosh, 2012). The cratering process creates a large non-coaxial shear force that rotates a plane that results in particles that flatten and elongate at the same time. This creates a lineation and a foliation. This has been observed in the shocked (S3) ordinary chondrite Pułtusk (Krzesińska et al., 2015). These investigators observed that the metal grains were plastically deformed and non-coaxially sheared into oblate and prolate shapes, whereas the silicates underwent brittle catalastic deformation defined by pseudotachylytes. The interesting result from that work is the coherence in their datasets with the alignment of magnetic, μCT orientation and planes. The similar alignment of Allende's lineation trends found in our study trace a foliation, with the shapes of particles being both oblate and prolate, could indicate than Allende has undergone a similar non-coaxial deformation. However, Allende has a lower shock value (S1) (Scott et al., 1992), which means the indicators of pseudotachylytes, and fracture sets that are associated with higher values shock do not exist. The high petrological type of Allende (>3.6, Bonal et al., 2006) could also anneal and destroy any brittle textures that could be diagnostic of such non-coaxial deformation.

Another possibility for the observed alignment of foliation and lineation in Allende could be due to the fact that the confining stresses of the rock surrounding the site of impact were heterogeneous, a point already suggested by MacPherson and Krot (2014) (Fig. 9). Such heterogeneity in the target material at the point of impact would not allow the material to deform in a purely oblate form, but it would also encourage flow into preferred dilatational fields creating a lineation. In addition to the work by MacPherson and Krot (2014), there is also textural evidence that the CV parent body was not homogeneous prior to impact; Mokoia $CV3_{OxA+OxB}$ is believed to be a breccia (Jones and Schilk, 2009; Kimura and Ikeda, 1998), in addition Vigarano $CV3_{Red\text{-}Ox}$ is a regolith breccia containing chondritic fragments in an interclastic matrix (MacPherson and Krot, 2014). It is unknown if the brecciation occurred due to the impact-related flattening event, a prior impact, or an accretionary event. One meteorite that does show previous brecciation prior to the flattening event is Vigarano $CV3_{Red+Ox}$ (Tomeoka and Kojima, 1998). This sequence is also consistent with observations of Leoville that has flattened breccia clasts indicating overprinting (Cain et al., 1986). Because the target materials of the CV parent body are not chemically or texturally uniform (as indicated by their redox sub-classification), and they likely contained variable amounts of porosity (Table 1), it stands to reason that they experienced mechanically non-uniform deformation as well. Such a mechanism introduces the possibility of preferred flow direction(s) (lineation). This lineation would occur as the pre-impact porosity collapses and the internal less competent grains deform as a response to an impact.

4.4. CV3 impact driven fluid migration model

It is noteworthy that existing textural evidence that supports the idea that fluids moved through chondrites is seen by the observation of "dish structures", which are convex bands of alteration that form around dark inclusions (Tomeoka and Kojima, 1998). On Earth, similar structures form in sediment that has undergone compaction (Tsuji and Miyata, 1987). If impacts mobilized fluids and led to secondary alteration then the timing of this alteration is important to understanding whether such a process could produce the observed differences of the "Ox" chondrite subtypes. Many studies place the timing of alteration after deformation (Keller et al., 1994; MacPherson and Krot, 2014; Rubin, 2012). The measured extinct radionuclides in some secondary minerals (Doyle et al., 2015), however, imply that the deformation was early. Evidence for ancient (4.54 Ga) impact events exists for some chondrite parent bodies (Righter et al., 2015), but radiogenic heating clearly also has an important role (Brearley and Krot, 2012).

In our CV parent body deformation model, fluids move through a medium by a pressure gradient (Carter et al., 1990), which is evidenced by the lineation observed in the Allende slab. The lineation does not necessarily cause fluids to migrate in a particular direction, but the interstitial fluids react to the pressure gradient (Fig. 9). This causes removal of fluids, which results in less alteration in the reduced CV types. In such a model, permeability may

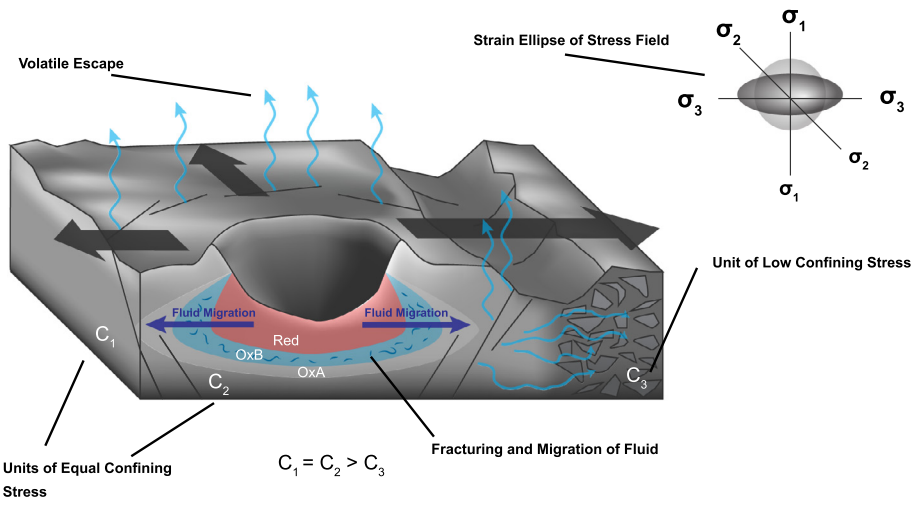

Fig. 9. Proposed model of lineation formation and fluid transport. This diagram illustrates a model for how the subtypes of CV chondrites ($CV_{red} < CV_{OxB} < CV_{OxA}$) may obtain their varying degrees of alteration. Upon impact of the chondrite parent body the heterogeneous confining pressures from the rock units (C_1–C_3) allow the formation of stress field towards the least competent rock unit (MacPherson and Krot, 2014). The gradient would direct fluid transport along that axis (indicated in the image as the blue "fluid migration axis"). Immediately following the impact, fluids are squeezed out of units experiencing the greatest shock following pore space collapse (CV_{red}). Intermediate units are faced with moderate pore space collapse and an influx of fluids, this leads to fracturing increasing permeability and alteration horizons (CV_{OxB}). Distal units are still deformed by the impact but retain a sizeable porosity and being in the pressure gradient also have an influx of fluids (CV_{OxA}). Pressure gradients would be exacerbated if faults (pre-existing or resulting from the impact) rupture at the surface and could lead to volatile loss from the parent body. (For interpretation of the references to color in this figure legend, the reader is referred to the web version of this article.)

limit transport of fluids, but they would travel into more porous rock units where the increase in porosity (i.e. surface area) allows greater effective alteration, such as the Ox_A and Ox_B subtypes. A preferred orientation to the pressure gradient would also result in the preferential transport of fluid(s) into one particular area, as compared to purely uniaxial deformation of uniformly competent target material leading to more equally dispersed alteration.

Wasson et al. (2013) and Lunning et al. (2016) attribute varying volatile concentrations and oxidation in CV, CK, CM chondrites to impact heating, generally consistent with the model outlined in this contribution. Notably, it is not easy to lose trace volatiles during thermal metamorphism of an internally heated body (i.e., one that was only heated by decay of ^{26}Al). Although the impact deformation model appears to generally explain the varying secondary alteration, volatile distribution, and possibly the oxidation in CV (and maybe CK) chondrites, we are not advocating the idea that a single impact deformation event was the cause or that all of the secondary mineralization or heating recorded by chondrites are due to impact processes. Future work finding microtextural evidence for the timing of petrofabric and secondary mineralization is needed to test and refine these ideas about the deformation history of chondrites and the proposed model. Nevertheless, a general outline of our conceptual model is as follows:

1) Starting parent body with heterogeneous composition of surface ices, rock and previously compacted units. Creating a target material with units of different starting competency (MacPherson and Krot, 2014).
2) Parent body is hit by a bolide, imposing uniaxial shortening in the immediate unit below and pore space collapse.
3) Residual heating, related to the impact causes melting of ices. Different porosities and rheological contrasts lead to differential compaction and give rise to a lateral pressure gradient (perpendicular to the uniaxial shortening direction).
4) This leads to fluid migration down pressure gradients away from the impact and 3D deformation of the compacting rock masses. The loss of oxidized fluids from the impact site and resultant lower porosity hinders further oxidation of the surrounding rock resulting in the reduced subtypes.
5) Adjacent to the impact, fluid influx will raise local pressure leading to hydraulic fracturing, increasing the exposed surface to oxidation by the inflowing fluids. Fluid injection increases pressure making localized resistance to pore space collapse in OxB subtypes. This increase of oxidized fluid and new surface area results in high oxidation, (OxB) subtypes.
6) Distal rocks have fluids injected into their ample pore space, melting further ices resulting in moderate oxidation and alteration, (OxA) subtypes.
7) Fractures from the impact or existing faults allow for fluids to migrate to the surface and escape the body resulting in volatile escape.

5. Conclusions

Allende $CV3_{OxA}$ has undergone significant shortening. This has resulted in planar and linear petrofabrics. It is likely that different particle phases in Allende reacted to stress heterogeneously, as indicated by the varying degrees of apparent shortening in CAIs ($64.5\%_{CT}$) > matrix ($21.5\%_{Fry}$) > chondrules ($17.6\%_{CT}$). The deformation of particles in Allende are largely consistent with the observed strain partitioning in other meteorites types such as the CM2 chondrite Murchison (Hanna et al., 2015) and predicted in computer modeling of the CV parent body (Bland et al., 2014). On top of a strong planar petrofabric, we found a penetrative linear fabric, which is evidence of a preferred flow direction during deformation. The common orientation of both the strike determined from the 2D analysis and the trend determined from the CT analysis represents an excellent agreement. We conclude that the presence of the lineation reveals mechanical heterogeneity in the CV parent body (MacPherson and Krot, 2014), or non-coaxial deformation (Krzesińska et al., 2015) resulting in a preferred orientation. Such a preferred orientation records a pressure gradient that would have more efficiently redistributed volatiles in the parent body. If the petrofabric formed from impact, resultant pressure gradients were likely produced. Analogous gradients exist on Earth and are known to migrate volatiles in the crust (Carter et al., 1990). We conclude that these structural controls on fluid migration inside parent bodies provide a credible mechanism that can help explain the origins of CV oxidized subtypes.

Acknowledgements

This work would not have been possible without the generous loan of a ~25 cm^2 slab of Allende CV3 and an adjacent slab from the personal collections of Joesph Minafra and Phil Mani. The Nondestructive Evaluation (NDE) Laboratory at NASA Johnson Space Center generously provided the Computed Tomography (CT) data. AWT and PS would like to thank the Lunar and Planetary Institute (LPI) and The National Aeronautics and Space Administration (NASA), for funding their 2013 and 2012 internships, through which this research was undertaken. In addition, KRF acknowledges his support through the NASA Co-op program. The research was supported by NASA Cosmochemistry Program grant 11-COS11-0066 to JIS who mentored AWT, KRF and PS as summer interns. We would like to thank Roberto Weinberg who reviewed an early version of this manuscript and provided valuable suggestions. We would lastly like to thank the feedback from Romy D. Hanna and two anonymous reviewers, whose comments greatly refined this paper.

Appendix A. Supplementary material

Supplementary material related to this article can be found online at http://dx.doi.org/10.1016/j.epsl.2016.09.015.

References

Allmendinger, R.W., Cardozo, N., Fisher, D., 2012. Structural Geology Algorithms: Vectors and Tensors in Structural Geology, 1st edn. Cambridge University Press.
Almeida, N.V., Smith, C.L., Sykes, D., Downes, H., Ahmed, F., 2015. Quantifying the deformation of Leoville chondrules in 3D: implications for the post-accretional history of the CV3 parent body. In: 78th Annual Meeting of the Meteoritical Society.
Bland, P.A., Collins, G.S., Davison, T.M., Abreu, N.M., Ciesla, F.J., Muxworthy, A.R., Moore, J., 2014. Pressure-temperature evolution of primordial solar system solids during impact-induced compaction. Nat. Commun. 5, 5451.
Bland, P.A., Howard, L.E., Prior, D.J., Wheeler, J., Hough, R.M., Dyl, K.A., 2011. Earliest rock fabric formed in the Solar System preserved in a chondrule rim. Nat. Geosci. 4, 244–247.
Bonal, L., Quirico, E., Bourot-Denise, M., Montagnac, G., 2006. Determination of the petrologic type of CV3 chondrites by Raman spectroscopy of included organic matter. Geochim. Cosmochim. Acta 70, 1849–1863.
Brearley, A.J., Krot, A.N., 2012. Metasomatism in the early solar system: the record from chondritic meteorites. In: Harlove, D.E., Austrheim, H. (Eds.), Metasomatism and Metamorphism: The Role of Fluids in Crustal and Upper Mantle Processes. Springer, Heidelberg, pp. 659–790.
Butler, R.F., 1992. Statistics of Paleomagnetic Data, Paleomagnetism: Magnetic Domains to Geologic Terranes. Blackwell Scientific, Boston, p. 319.
Cain, P.M., McSween Jr., H.Y., Woodward, N.B., 1986. Structural deformation of the Leoville chondrite. Earth Planet. Sci. Lett. 77, 165–175.
Cardozo, N., Allmendinger, R.W., 2013. Spherical projections with OSXStereonet. Comput. Geosci. 51.
Carter, N.L., Kronenberg, A.K., Ross, J.V., Wiltschko, D.V., 1990. Controls of fluids on defomration of rocks. Geol. Soc. (Lond.) Spec. Publ. 54, 1–13.
Corrigan, C.M., Zolensky, M.E., Dahl, J., Long, M., Weir, J., Sapp, C., Burkett, P.J., 1997. The porosity and permeability of chondritic meteorites and interplanetary dust particles. Meteorit. Planet. Sci. 32, 509–515.
Dodd Jr., R.T., 1965. Preferred orientation of chondrules in chondrites. Icarus 4, 308–316.
Doube, M., Kłosowski, M.M., Arganda-Carreras, I., Cordelières, F.P., Dougherty, R.P., Jackson, J.S., Schmid, B., Hutchinson, J.R., Shefelbine, S.J., 2010. BoneJ: free and extensible bone image analysis in ImageJ. Bone 47, 1076–1079.
Doyle, P.M., Jogo, K., Nagashima, K., Krot, A.N., Wakita, S., Ciesla, F.J., Hutcheon, I.D., 2015. Early aqueous activity on the carbonaceous and ordinary chondrite parent asteroids recorded by secondary fayalite. Nat. Commun. 6.
Fisher, R., 1953. Dispersion on a sphere. Proc. R. Soc. Lond. A 217, 295–305.
Flinn, D., 1962. On folding during three-dimensional progressive deformation. Q. J. Geol. Soc. 118, 385–428.
Fry, N., 1979. Random point distributions and strain measurement in rocks. Tectonophysics 60, 89–105.
Gattacceca, J., Rochette, P., Denise, M., Consolmagno, G., Folco, L., 2005. An impact origin for the foliation of chondrites. Earth Planet. Sci. Lett. 234, 351–368.
Hanna, R.D., Ketcham, R.A., Zolensky, M., Behr, W.M., 2015. Impact-induced brittle deformation, porosity loss, and aqueous alteration in the Murchison CM chondrite. Geochim. Cosmochim. Acta 171, 256–282.
Ivanova, M.A., Lorenz, C.A., Shuvalov, V.V., Krot, A.N., Macpherson, G.J., Bizzarro, M., 2014. Plastically-deformed igneous calcium–aluminum-rich inclusions from CV carbonaceous chondrites: clues to a nature of CAI melting events. In: 45th Lunar and Planetary Science Conference. The Woodlands, TX, USA.
Jones, R.H., Schilk, A.J., 2009. Chemistry, petrology and bulk oxygen isotope compositions of chondrules from the Mokoia CV3 carbonaceous chondrite. Geochim. Cosmochim. Acta 73, 5854–5883.
Keller, L.P., Thomas, K.L., Clayton, R.N., Mayeda, T.K., DeHart, J.M., McKay, D.S., 1994. Aqueous alteration of the Bali CV3 chondrite: evidence from mineralogy, mineral chemistry, and oxygen isotopic compositions. Geochim. Cosmochim. Acta 58, 5589–5598.
Kimura, M., Ikeda, Y., 1998. Hydrous and anhydrous alterations of chondrules in Kaba and Mokoia CV chondrites. Meteoritics 33, 1139–1146.
Kornacki, Alan S., Wood, John A., 1984. Petrography and classification of Ca, Al-rich and olivine-rich inclusions in the Allende CV3 chondrite. J. Geophys. Res. 89, B573–B587.
Krzesińska, A., Gattacceca, J., Friedrich, J.M., Rochette, P., 2015. Impact-related noncoaxial deformation in the Pułtusk H chondrite inferred from petrofabric analysis. Meteorit. Planet. Sci. 50, 401–417.
Lunning, N.G., Corrigan, C.M., McSween Jr., H.Y., Tenner, T.J., Kita, N.T., Bodnar, R.J., 2016. CV and CM chondrite impact melts. Geochim. Cosmochim. Acta 189, 338–358.
Macke, R.J., Britt, D.T., Consolmagno, G.J., 2011a. Density, porosity and magnetic susceptibility of achondritic meteorites. Meteorit. Planet. Sci. 46, 3110326.
Macke, R.J., Britt, D.T., Consolmagno, G.J., 2011b. Density, porosity and magnetic susceptibility of carbonaceous chondrites. Meteorit. Planet. Sci. 46, 1842–1862.
MacPherson, G.J., Grossman, L., 1984. "Fluffy" type A Ca-, Al-rich inclusions in the Allende meteorite. Geochim. Cosmochim. Acta 48, 29–46.
MacPherson, G.J., Krot, A.N., 2014. The formation of Ca-, Fe-rich silicates in reduced and oxidized CV chondrites: the roles of impact-modified porosity and permeability, and heterogeneous distribution of water ices. Meteorit. Planet. Sci. 49, 1250–1270.
Martin, P.M., Mills, A.A., 1976. Size and shape of chondrules in the Bjurböle and Chainpur meteorites. Earth Planet. Sci. Lett. 33, 239–248.
Martin, P.M., Mills, A.A., Walker, E., 1975. Preferential orientation in four C3 chondritic meteorites. Nature 257, 37–38.
McNamara, K., Schneberk, D.J., Empey, D.M., Koshti, A., Pugel, D.E., Cozmuta, I., Stackpoole, M., Ruffino, N.P., Pompa, E.C., Oliveras, O., Kontinos, D.A., 2010. X-Ray computed tomography inspection of the stardust heat shield. In: International Planetary Probe Workshop.
McSween, H.Y., 1977. Petrographic variations among carbonaceous chondrites of the Vigarano type. Geochim. Cosmochim. Acta 41, 1777–1790.
Melosh, H.J., 2012. The contact and compression stage of impact cratering. In: Osinski, G.R., Pierazzo, E. (Eds.), Impact Cratering: Processes and Products. Wiley–Blackwell, p. 330.
Palin, R.M., Weller, O.M., Waters, D.J., Dyck, B., 2015. Quantifying geological uncertainty in metamorphic phase equilibria modelling; a Monte Carlo assessment and implications for tectonic interpretations. Geosci. Front.
Passchier, C., Trouw, R., 2005. Microtectonics, 2nd edn. Springer.
Piazolo, S., Passchier, C.W., 2002. Controls on lineation development in low to medium grade shear zones: a study from the Cap de Creus peninsula, NE Spain. J. Struct. Geol. 24, 25–44.
Righter, K., Abell, P., Agresti, D., Berger, E.L., Burton, A.S., Delaney, J.S., Fries, M.D., Gibson, E.K., Haba, M.K., Harrington, R., Herzog, G.F., Keller, L.P., Locke, D., Lindsay, F.N., McCoy, T.J., Morris, R.V., Nagao, K., Nakamura-Messenger, K., Niles, P.B., Nyquist, L.E., Park, J., Peng, Z.X., Shih, C.Y., Simon, J.I., Swisher, C.C., Tappa, M.J., Turrin, B.D., Zeigler, R.A., 2015. Mineralogy, petrology, chronology, and exposure history of the Chelyabinsk meteorite and parent body. Meteorit. Planet. Sci. 50, 1790–1819.
Rubin, A.E., 2012. Collisional facilitation of aqueous alteration of CM and CV carbonaceous chondrites. Geochim. Cosmochim. Acta 90, 181–194.
Schneider, C.A., Rasband, W.S., Eliceriri, K.W., 2012. NIH image to ImageJ: 25 years of image analysis. Nat. Methods 9, 671–675.
Scott, E.R.D., Keil, K., Stöffler, D., 1992. Shock metamorphism of carbonaceous chondrites. Geochim. Cosmochim. Acta 56, 4281–4293.
Simon, S.B., Grossman, L., Casanova, I., Symes, S., Benoit, P., Sears, D.W.G., Wacker, J.F., 1995. Axtell, a new CV3 chondrite find from Texas. Meteorit. Planet. Sci. 30, 42–46.
Sneyd, D.S., McSween, J.H.Y., Labotka, T.C., 1985. Strain analysis of the parnallee unequilibrated ordinary chondrite. In: 16th Annual Lunar and Planetary Science Conference, pp. 797–798.
Sneyd, D.S., McSween Jr., H.Y., Sugiura, N., Strangway, D.W., Nord, J.G.L., 1988. Origin of petrofabrics and magnetic anisotropy in ordinary chondrites. Meteoritics 23, 139–149.
Tomeoka, K., Kojima, T., 1998. Arcuate band texture in a dark inclusion from the Vigarano CV3 chondrite: possible evidence for early sedimentary processes. Meteorit. Planet. Sci. 33, 519–525.
Tsuji, T., Miyata, Y., 1987. Fluidization and liquefaction of sand beds: experimental study and examples from Nichinan group. J. Geol. Soc. Jpn. 93, 791–803.
Waldron, J.W.F., Wallace, K.D., 2007. Objective fitting of ellipses in the centre-to-

centre (fry) method of strain analysis. J. Struct. Geol. 29, 1430–1444.
Wasson, J.T., Isa, J., Rubin, A.E., 2013. Compositional and petrographic similarities of CV and CK chondrites: a single group with variations in textures and volatile concentrations attributable to impact heating, crushing and oxidation. Geochim. Cosmochim. Acta 108, 45–62.
Watt, L.E., Bland, P.A., Prior, D.J., Russell, S.S., 2006. Fabric analysis of Allende matrix using EBSD. Meteorit. Planet. Sci. 41, 989–1001.
Weinberg, R.F., Hasalova, P., Ward, L., Fanning, C.M., 2013. Interaction between deformation and magma extraction in migmatites: examples from Kangaroo Island, South Australia. Geol. Soc. Am. Bull.